New York) supplemented with 10% fetal bovine serum (FBS) and 1% penicillin/streptomycin. The cultures were kept in a humidified atmosphere containing 5% $CO_2$ and 95% air at 37°C. Nonadherent cells were removed after 24 h. Adherent cells were trypsinized with 0.25% trypsin-EDTA (Gibco), harvested and then plated into new flasks at every 90% confluency. Adherent mesenchymal stromal cells (MSCs) from passage 2 were frozen in liquid nitrogen for future use. Early passage cells were examined for their capacity to differentiate in culture.

For the *in vitro* differentiation assay, passage 4 MSCs were tested for their ability to differentiate into osteocytes and adipocytes.[21] For adipocyte differentiation, cells ($2 \times 10^5$) were cultured with Differentiation Media Bullet Kit-Adipogenic (Lonza, Basel, Switzerland) according to the manufacturer's instructions. MSCs were cultured in 6-well plates with MSC culture medium until they reached confluency. Cells were then exposed to three cycles of adipogenic induction medium alternating with adipogenic maintenance medium. Following three complete cycles of induction/maintenance, the MSCs were cultured for 7 more days in supplemented adipogenic maintenance medium. Cell differentiation to adipocytes was confirmed by Oil Red O (Muto Chemicals, Tokyo, Japan) staining. For osteogenic differentiation, cells ($2 \times 10^4$) were plated and the culture medium was replaced with Differentiation Media Bullet Kit-Osteogenic (Lonza) until confluence. Cells were stained with alizarin red S (Wako Pure Chemicals).

Primary hepatocytes from swine liver were prepared by the conventional perfusion method with collagenase digestion. Hepatocytes were seeded at $3 \times 10^6$ cells per dish in 10-cm-diam plastic dishes and cultured in William's E complete medium (Gibco, Grand Island, New York) supplemented with 10% FBS, 1-nM insulin, and 1-nM dexamethasone in a humidified atmosphere of 5% $CO_2$/95% air at 37°C.

### 2.5 *Flow Cytometry*

Peripheral blood cells were isolated from 10 ml of freshly drawn heparinized blood of pigs, and red cells were lysed in a buffer containing 155-mM $NH_4Cl$, 10-mM $KHCO_3$ and 0.1-mM EDTA. Precipitated white cells were resuspended in 0.1% FBS-PBS, and cells were analyzed using FACSCalibur (Beckton Dickinson, Mountain View, California) and FlowJo analysis software (Tree Star, San Carlos, California).

### 2.6 *Histological Analysis, Nissl Staining, and Hematoxylin and Eosin staining*

Three male GFP-Tg Jinhua cloned pigs were used for histological observations. Animals (8 to 36 months, weighing approximately 70 to 120 kg) were deeply anesthetized by inhalation of isoflurane (4% 1 L/min, Dinippon Pharmaceutical Company, Osaka, Japan) and intramuscular injection of domitor (0.6 mL, Meiji seika, Tokyo, Japan) and dormicum (0.6 mL, Astellas Pharma, Tokyo, Japan). Tissues (brain, pancreas, skeletal muscle, cardiac muscle, small intestine, stomach, liver, colon, and testis) were isolated from anesthetized Tg animals and fixed in 4% paraformaldehyde (Merck KGaA, Darmstadt, Germany) with 0.1-M phosphate buffer (pH 7.4). Tissue samples were soaked in 20% sucrose in PBS at 4°C for 2 to 4 days, frozen in OCT compound (Tissue-Tek, Sakura Finetechnical Company, Tokyo, Japan), and then sectioned at a thickness of 10 to 40 μm using a cryostat (Leica CM 1850, Leica Incorporated, Nussloch, Germany). Sections were then mounted onto silane-coated slides.

To identify the cell architecture of the brain, delipidated brain sections were immersed in 0.1% solution of Cresylecht violet (Chroma-Gesellschaft, Munster, Germany) overnight at 37°C (Nissl staining). Slides were dehydrated through graded ethanol baths, delipidated in xylene, and then mounted with Mount-Quick (Daidosangyo Company, Tokyo, Japan).

For hematoxylin and eosin (HE) staining, all samples except for brain were embedded in paraffin (Wako Pure Chemicals) and then sectioned at a thickness of 4 μm using a sliding microtome (REM-700, Yamato Kohki Industrial Company, Saitama, Japan). Sections were deparaffinized, rehydrated to water, and then stained with hematoxylin (Wako Pure Chemicals) and eosin (Wako Pure Chemicals).

All frozen sections except for brain were counterstained with DAPI (Sigma Chemical, Saint Louis, Missouri). GFP fluorescence was examined using a fluorescent microscope Keyence BZ-9000 (Keyence, Tokyo, Japan). Micrographs were taken using a digital camera attached to the same microscope. Digital images were processed with Adobe Photoshop CS2 to adjust the final plates.

### 2.7 *Survey of Reproductive and Growth Performance in Green Fluorescent Protein Pigs*

A primary GFP Jinhua pig mated with wild-type Jinhua boars and farrowed the second generation of GFP-Tg piglets (three litters). Boars of the second generation mated with five wild-type Jinhua sows and the sows farrowed the third generation.

For surveillance of reproductive and growth performance in GFP-Tg Jinhua pigs, pregnant pigs that conceived GFP pigs entered the farrowing unit 1 week before the expected date of parturition and were housed in an individual section (1.2 × 2.5 m) of a slated barn until weaning. Piglets were weaned at 30 days of age. After weaning, piglets were reared in pens (2.4 × 2.5 m) for each litter. Each pen had a feeder and water cup that allowed free access to feed (18% crude protein, 3080 kcal/kg digestible energy) and water throughout the experiment. The body weight of piglets was recorded every week until they reached two months of age.

### 2.8 *Statistical Analyses*

All statistical analyses were performed with StatView software (Windows©version 5; SAS Institute Incorporated, Cary, North Carolina). Data concerning born-alive rate (number born alive/number of total born) and weaning rate (number of weaning piglets/number born alive) between GFP-positive and GFP-negative piglets were analyzed by a Fisher's exact test. Data regarding body weight of piglets were analyzed using two-way factorial ANOVA and the Tukey-Kramer multiple range test.

## 3 Results

### 3.1 *Generation of Green Fluorescent Protein Expressing Cloned Pigs*

Primary fibroblasts from the skin (4-day-old female Jinhua pig) were isolated and grown for transgenic donor cells. The liner pEGFPneo plasmid DNA (10 μg) was transduced with

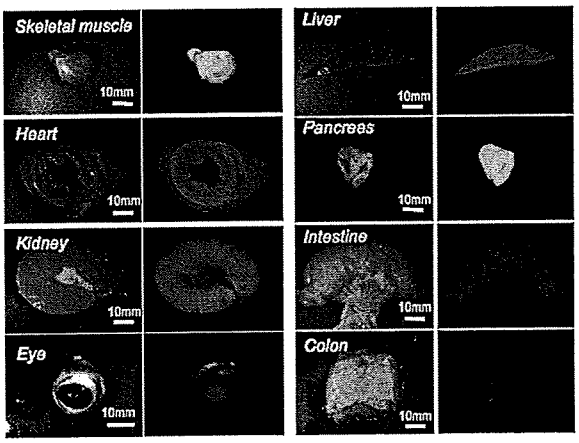


Fig. 2 Macroscopic GFP expression profile in various organs from cloned pigs. Representative organs (skeletal muscle, heart, kidney, eye, liver, pancreas, small intestine, and colon) were removed from GFP-expressing pigs and macroscopically examined under a visible (left) or 489-nm excitation (right) light. Results derived from one of two independent experiments showing similar results.

primary fibroblasts using an electroporation system. After G418 selection for 2 weeks, 212 colonies (18.0%) of 1177-sorted cells were grown to confluence in 35-mm culture dishes. One of the cell lines that expressed a strong GFP signal was used for nuclear transfer [Fig. 1(c)]. 23 (9.2%) of 249 somatic cell nuclear transferred oocytes developed to the morula-blastocyst stage 110 h after nuclear transfer. These morula-blastocysts (average 7.7/recipient) were cotransferred with parthenogenetic embryos (average 17.3/recipient) into three recipient gilts, two of which became pregnant and each farrowed a total of two piglets (8.7%: 2/23) at day 113 after nuclear transfer. Both of the two cloned Jinhua pigs possessed GFP-specific sequences according to PCR analysis [Fig. 1(d)]. Visual inspection under an excitation light demonstrated that GFP-derived fluorescence was clearly expressed in the skin, oral and nasal mucosa, and hoof wall of the transgenic pigs [Fig. 1(e)].

### 3.2 *Green Fluorescent Protein Expression Pattern in the Newly Created Cloned Pig*

In an effort to examine the expression pattern of newly generated cloned pigs, various organs were removed from the transgenic pigs and their macroscopic expression pattern was determined (Fig. 2). While skeletal muscle and pancreas showed strong GFP expression in the cloned pigs, expression in gastrointestinal tracts and eyes was weak in comparison. GFP signals in the kidney and liver of cloned pigs appeared moderate and heterogeneous.

We further analyzed microscopic GFP expression patterns in various organs (Table 1 and Figs. 3–5). GFP expression sites in the central nervous system (CNS) are summarized in Fig. 3. Nisslstaining was also performed to identify the cell architecture of the brain [Figs. 4(a)–4(k)]. Small-sized and round-shaped GFP-positive cell bodies were found in the olfactory bulb [Figs. 3(a) and 4(d)], lateral ventricle [Figs. 3(b), 3(c), 4(g), and 4(h)], and hippocampus [Figs. 3(c) and 4(f)].

**Table 1** Expression profile of GFP-expressing Jinhua pigs. GFP expression was determined microscopically under a 489-nm excitation light.

| GFP expression | Tissues/cells |
|---|---|
| Very strong (+++) | Skeletal muscle, heart, pancreas, thyroid gland |
| Strong (++) | Epidermis (skin), tongue, oral mucosa, liver, kidney, brain, lung |
| Moderate (+) | Spleen, stomach, small intestine, colon, thymus, testis, ovary, eye, bone, cartilage, vessels |
| Negative (−) | Connective tissue (dermis), erythrocyte, sperm |

In contrast, large-sized cell bodies were observed in the cerebellum [Fig. 4(j)]. Both large- and small-sized cell bodies were found in the medula oblongata [Fig. 4(l)]. GFP-positive fibers were found in the olfactory bulb [Figs. 4(b) and 4(d)], cerebellum [Fig. 4(j)], and medula oblongata [Fig. 4(l)].

GFP expression of the skin was predominant in the epidermis (the granular layer and stratum spinosum) and the hair follicle, but less so in the dermis [Figs. 5(a) and 5(b)]. Expression in skeletal [Figs. 5(c) and 5(d)] and cardiac muscle [Figs. 5(e) and 5(f)] appeared modestly heterogeneous, but most of the muscle fibers were GFP-positive. Regarding expression in the liver, parenchymal cells appeared GFP-positive and interstitial cells were GFP-negative [Figs. 5(g) and 5(h)]. Acinus cells in the pancreas were strongly GFP-positive [Figs. 5(i) and 5(j)]. In the gastrointestinal tract, GFP was heterogeneously expressed in the epithelium of the stomach, intestine, and colon [Figs. 5(k)–5(p)]. Primary and secondary spermatocytes in the testis weakly expressed GFP, al-

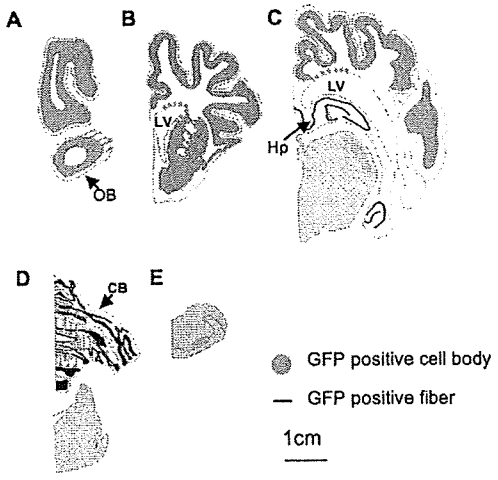


Fig. 3 Schematic illustration of GFP expression sites in the brain of cloned pigs. Coronal sections are illustrated from (a) rostral to (e) caudal. The green circle represents GFP-positive cell bodies and the red line indicates GFP-positive fibers. (Color online only.)

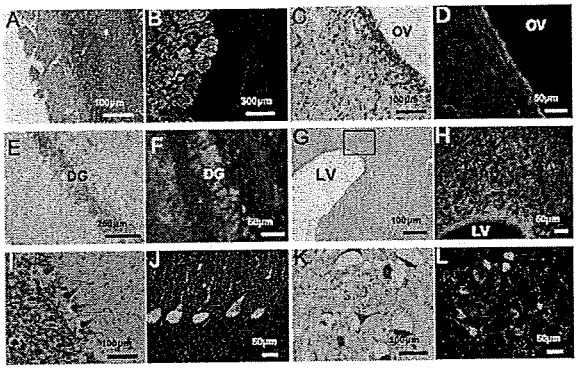


Fig. 4 Photomicrographs of GFP fluorescence and Nissl-staining in the brain of cloned pigs. (a) to (d) olfactory bulb; (e) and (f) hippocampus; (g) and (h) lateral ventricle; (i) and (j) cerebellum; (k) and (l) medula oblongata. (a), (c), (e), (g), (i), and (k): Nissl staining. (b), (d), (f), (h), (j), and (k): 489-nm excitation light.

though sperms were almost totally GFP-negative [Figs. 5(q) and 5(r)]. Since it is important to know the fate of leukocytes in many biomedical studies, we examined GFP expression of peripheral blood cells from cloned pigs [Figs. 5(s) and 5(t)]. Leukocytes were GFP-positive, granulocytes exhibited a particularly strong expression of GFP, and mononuclear cells were also moderately GFP-positive. Notably, GFP expression of erythrocytes was definitely negative. FACS analysis also revealed strong GFP expression in peripheral leukocytes [Fig. 5(u)].

### 3.3 *Green Fluorescent Protein Expression in Potential Cell Sources*

To restore form and function to damaged tissues, a cell transplantation strategy has emerged as a potential therapeutic approach involving the use of autologous cells. Therefore, we examined GFP expression in the processed cells for transplantation (Fig. 6). Since mesenchymal stem cells (MSCs) possess a high expansion potential and genetic stability[22] and can be easily isolated and transferred from the laboratory to the bedside, we first examined GFP expression in bone-marrow-derived MSCs. As shown in Fig. 6(a), sufficient levels of GFP expression were observed in isolated MSCs. The cells rapidly proliferated and formed colonies, and GFP expression levels were not altered, even within several cell passages (data not shown). These cells were capable of differentiating successfully into osteocytes [Fig. 6(c)], but poorly into adipocytes [Fig. 6(b)]. These results demonstrate that GFP expression was stable in MSCs from cloned pigs and preferentially differentiated into osteocytes. We next addressed GFP expression in cultured parenchymal hepatocytes from the cloned pigs [Figs. 6(d)–6(f)]. Sufficient levels of GFP expression were observed in proliferating hepatocytes, but not in adherent hepatocytes with the contact inhibition. A similar phenomenon was observed in Langerhans islets isolated from cloned pig pancreas [Figs. 6(g)–6(i)].

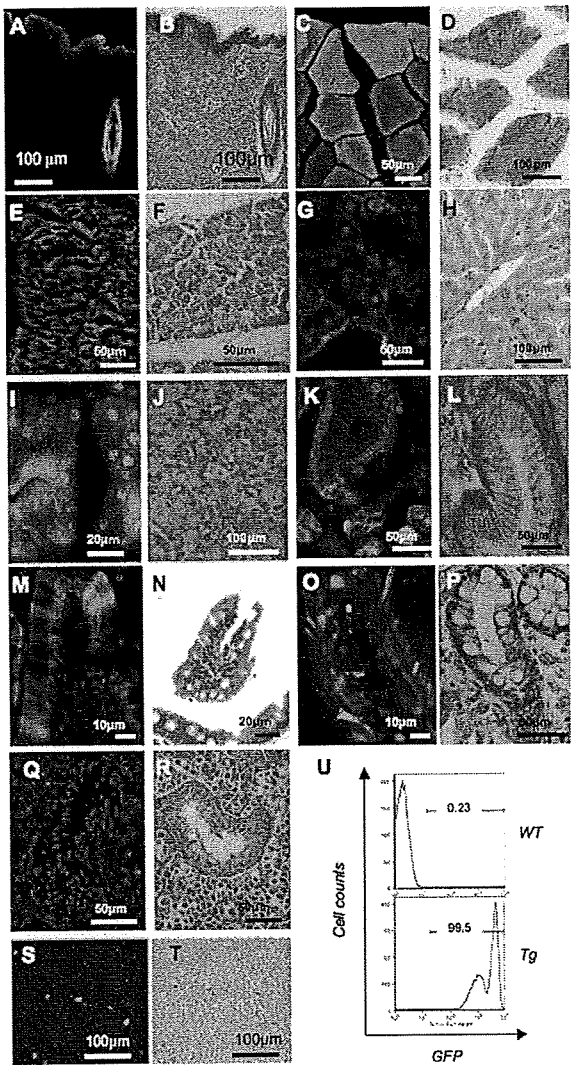


Fig. 5 Microscopic GFP expression in representative tissue sections from cloned pigs other than brain. (a), (c), (e), (g), (i), (k), (m), (o), and (q) Representative tissue sections (skin, skeletal muscle, cardiac muscle, liver, pancreas, stomach, small intestine, colon, and testis) from GFP-expressing pigs were inspected under 489-nm excitation light HE staining: (b), (d), (f), (h), (j), (l), (n), (p), and (r). (s) and (t) Hemogram of peripheral blood from a GFP-Tg pig. Leukocytes (granulocytes and mononuclear cells) expressed GFP, although erythrocytes showed no expression. (s) 489-nm excitation light; (t) visible light. (u) Representative flow-cytometrical GFP-expression pattern in peripheral blood leukocytes. More than 90% of leukocytes were GFP-positive. WT, leukocytes from a wild-type pig; Tg, leukocytes from a GFP-transgenic pig. Results derived from one of two independent experiments showing similar results.

### 3.4 *Reproductive Performance of Green Fluorescent Protein Jinhua Pigs*

A piglet of GFP-cloned piglets died 2 days after birth, but the remainder grew up normally and expressed estrus. The primary GFP-cloned female mated with a wild-type boar by artificial insemination and farrowed the second generation of

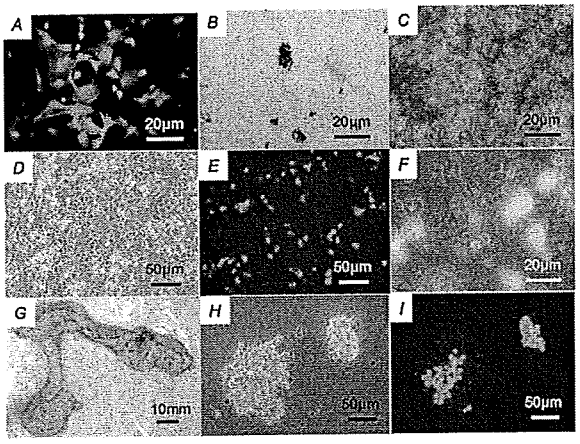


Fig. 6 GFP expression in potential cellular sources. (a) Strong GFP expression in bone-marrow-derived MSCs from the GFP-transgenic pig. Under appropriate differentiation conditions, MSCs were capable of differentiating into (c) adipocytes (stained with Oil red O for lipid droplets) and (d) osteocytes (stained with alizarin red for mineral deposition). Original magnification 20×. (d), (e), and (f) GFP expression in cultured parenchymal hepatocytes from cloned pigs. (d) Visible light, (e) excitation light. (f) Representative merged image of GFP-expressing cultured hepatocytes. (g) Visual inspection of the pancreas of cloned pigs (visible light). Langerhans islets isolated from the cloned pig pancreas were cultured and GFP expression was examined under (h) a visible and (i) 489-nm excitation light (original magnification 200×). (Color online only.)

A

| Reproductive performance of GFP cloned pig | | | |
|---|---|---|---|
| Litter number | Litter size | Number of GFP positive (%) | Number of weaned piglets |
| 1 | 8 | 3 (37.5) | 8 |
| 2 | 14 | 8 (57.1) | 12 |
| 3 | 11 | 6 (54.5) | 9 |
| Average | 11 | 5.7 (51.5) | 9.7 |

B

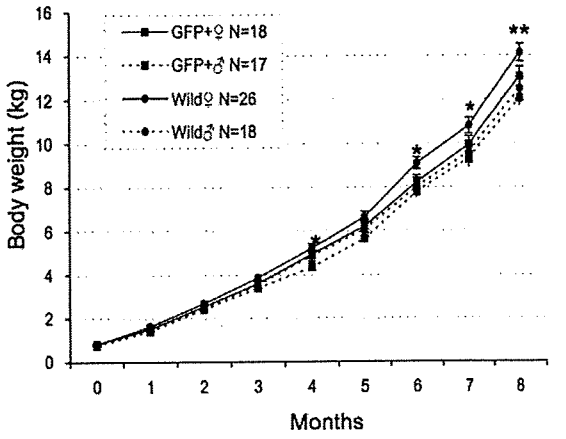


Fig. 7 Reproductive and growth performance of GFP-expressing pigs. (a) Summary of average litter size and average number of weaned piglets in three parities. (b) Growth performance of GFP cloned pigs. GFP, GFP cloned pigs. Wild, wild-type pigs; ♀, female; ♂, male. The female is heavier than the male after reaching 4 months of age (4, 6, and 7 weeks: *, $p < 0.05$; 8 weeks: **, $p < 0.01$).

GFP pigs. The average litter size and average number of weaned piglets in three parities were 11 and 9.7, respectively [Fig. 7(a)]. To examine the GFP expression rate in the second generation, PCR analysis and inspection by excitation light were also performed. The results showed that the GFP expression rate was 51.5% (17/33). Two boars of second-generation GFP Jinhua pigs mated with five females of wild-type pigs. The third generations (total 52 piglets) were born and 22 (42.3%) of these individuals were GFP-positive in genotype and phenotype. These results indicate that reproductive activity is successfully maintained in the established GFP-cloned Jinhua pigs, and that the introduced GFP transgene can be stably transmitted to pigs in subsequent generations.

### 3.5 *Growth Performance of Green Fluorescent Protein Transgenic Pigs*

We further evaluated the influence of the GFP transgene on growth performance of GFP-Tg pigs. A total of 85 piglets (33 of second-generation and 52 of third-generation piglets) were examined using body weight. The born-alive rate in GFP-positive and -negative pigs was 89.7% (35/39) and 95.7% (44/46), respectively. The weaning rate in GFP positive and negative piglets was 100% (35/35) and 97.7% (43/44), respectively. There were no differences between GFP-positive and -negative piglets for born-alive and weaning rates. The body weights of 79 born-alive piglets did not differ between GFP-positive and -negative piglets, while the female was heavier than the male after 4 months of age (4, 6, and 7 weeks: $P < 0.05$; 8 weeks: $P < 0.01$) [Fig. 7(b)]. As with wild-type Jinhua pigs, the body size of GFP-positive piglets reached plateau levels around 24 months (male: 96.0 ± 4.7 kg [n = 8]; female: 107.6 ± 13.3 kg [n = 12]), and the miniature size was maintained. These results demonstrate that the GFP transgene has less effect on growth performance of Tg pigs.

## 4 Discussions

We created new GFP-expressing pigs using a somatic cell cloning technique. The remarkable features presented as an imaging source include: 1. the born GFP-Tg pig demonstrated an organ/tissue-dependent expression pattern; 2. it displayed normal growth and fertility; and 3. the introduced GFP gene was transmitted to pigs in subsequent generations. The new GFP-expressing Jinhua pigs could provide new cellular/tissue light sources for biological imaging.

The Jinhua pig is a kind of indigenous Chinese pig.[23] The growth and reproductive traits of this pig were evaluated using microsatellite markers.[24,25] It has been reported that the mean litter size is 11 piglets, and that the pig shows premature growth and high multiplication.[26,27] The adult body weight of Jinhua pigs ranges from 90 to 110 kg (data not shown). Although Jinhua pigs have sufficient reproductive ability, the pigs have not been used as a commercial base resource [due to the low carcass lean content (29 to 30%) compared with large white pigs (53 to 54%).[27] However, since Jinhua pigs

exhibit a middle body size similar to the human body size, organs from this breed may represent an appropriate organ resource of xeno-transplantation for humans.

GFP expression was observed in various organs in this study, although expression levels differed between tissues/organs. It is very important for researchers to know the expression profile for various tissues/organs, because it is impossible to regulate the integration site and the copy number of transgenes into the genome in transgenic animals.[2,22] Since our previous results demonstrated that naked GFP-expression plasmid DNA was successfully expressed in the pig liver,[28] this general promoter and enhancer could be driven in various tissues/organs of cloned pigs. In particular, GFP expression was strong in the skeletal muscle, pancreas, heart, and kidney. These organs are potentially available for organ transplantation experiments as in the case of rats.[2] In terms of experimental cell therapy, it may also be possible to use neural progenitor cells. However, the culture system for pig neural progenitor cells may be required for future *in vivo* animal experiments, whereas the system for cell culture and large-animal experiments remains to be established. At the very least, MSCs, hepatocytes, and islet cells of the pancreas seem to be available for cell transplantation studies.

The present study demonstrated that an introduced GFP gene was very stable in Jinhua pigs, and that it was transmitted to the second and third generations. The first sow transmitted the gene to the second generation (both male and female pigs), and the second-generation male pig transmitted it to the third generation (both male and female pigs), suggesting a stable genotype and phenotype transmission. This also allows us to preserve this animal source as a fertilized egg and/or sperm.

The cells used for the nuclear transfer in this study were grown in culture from one cell of fibroblasts, and they had eventually divided around 20 times. Nevertheless, the evidence that normal individual pigs were successfully generated suggests that somatic cells of the pig may be resistant to gene alterations, including epigenetic mutations, in comparison with other animals such as cows.[29–32] This may represent a species-specific characteristic.

As indicated in Fig. 7(a), the GFP-transmission rate was around 50% from the sow to the second generation. This suggests the transduced gene was integrated into one portion of a chromosome. It was thought that gene transmission by this somatic cell cloning technique was almost totally equivalent to the case of intracytoplasmic sperm injection-mediated DNA transfer.[33] This study also demonstrated that the GFP gene did not influence the growth or reproduction of the cloned pig greatly. Since the GFP-Tg pigs were maintained in hemizygous conditions in the present study, any influence under homozygous conditions remains to be elucidated.

In conclusion, new GFP-expressing pigs showed normal growth and stable reproductive activity. Taking advantage of stable light sources, the GFP expression profile in these pigs may provide useful imaging information in research fields such as tissue engineering, experimental regenerative medicine, and transplantation.

## Acknowledgments

We would like to thank S. Kashiwazaki (University of Tsukuba, Japan) for donating pCX-GFP and pGKNeoPolyA/pUC19 plasmids. This study was supported by a research grant to author Kawarasaki from Shizuoka Prefecture, a grant to Kobayashi from the Japan Society for the Promotion of Science (project number 18300143; 2006-2008), and Health and Labour Science Research grants from the Ministry of Health, Labor and Welfare, and by a grant from the "Strategic Research Platform" Project for Private Universities: matching fund subsidy from the Ministry of Education, Culture, Sports, Science and Technology of Japan (2008).

## References

1. R. Weissleder and M. J. Pittet, "Imaging in the era of molecular oncology," *Nature (London)* **452**(7187), 580–589 (2008).
2. T. Murakami and E. Kobayashi, "Color-engineered rats and luminescent LacZ imaging: a new platform to visualize biological processes," *J. Biomed. Opt.* **10**(4), 41204 (2005).
3. J. Lippincott-Schwartz and G. H. Patterson, "Development and use of fluorescent protein markers in living cells," *Science* **300**(5616), 87–91 (2003).
4. R. M. Hoffman, "The multiple uses of fluorescent proteins to visualize cancer in vivo," *Nat. Rev. Cancer* **10**(10), 796–806 (2005).
5. R. Takahashi, T. Kuramochi, K. Aoyagi, S. Hashimoto, I. Miyoshi, N. Kasai, Y. Hakamata, E. Kobayashi, and M. Ueda, "Establishment and characterization of CAG/EGFP transgenic rabbit line," *Transgenic Res.* **16**(1), 115–120 (2007).
6. A. K. Mothe, I. Kulbatski, R. L. van Bendegem, L. Lee, E. Kobayashi, A. Keating, and C. H. Tator, "Analysis of green fluorescent protein expression in transgenic rats for tracking transplanted neural stem/progenitor cells," *J. Histochem. Cytochem.* **53**(10), 1215–1226 (2005).
7. Y. Yamaguchi, T. Kubo, T. Murakami, M. Takahashi, Y. Hakamata, E. Kobayashi, S. Yoshida, K. Hosokawa, K. Yoshikawa, and S. Itami, "Bone marrow cells differentiate into wound myofibroblasts and accelerate the healing of wounds with exposed bones when combined with an occlusive dressing," *Breast Cancer Res. Treat.* **152**(4), 616–622 (2005).
8. T. Shimizu, H. Sekine, J. Yang, Y. Isoi, M. Yamato, A. Kikuchi, E. Kobayashi, and T. Okano, "Polysurgery of cell sheet grafts overcomes diffusion limits to produce thick, vascularized myocardial tissues," *FASEB J.* **20**(6), 708–710 (2006).
9. J. S. Francis, A. Olariu, E. Kobayashi, and P. Leone, "GFP-transgenic Lewis rats as a cell source for oligodendrocyte replacement," *Exp. Neurol.* **205**(1), 177–189 (2007).
10. C. V. Hunter, L. S. Tiley, and H. M. Sang, "Developments in transgenic technology: applications for medicine," *Trends Mol. Med.* **11**(6), 293–298 (2005).
11. L. M. Houdebine, "Transgenic animal models in biomedical research," *Methods Mol. Biol.* **360**, 163–202 (2007).
12. H. Niemann, X. C. Tian, W. A. King, and R. S. Lee, "Epigenetic reprogramming in embryonic and foetal development upon somatic cell nuclear transfer cloning," *Reproduction* **135**(2), 151–163 (2008).
13. L. Tesson, J. Cozzi, S. Menoret, S. Remy, C. Usal, A. Fraichard, and I. Anegon, "Transgenic modification of the rat genome," *Transgenic Res.* **14**(5), 531–546 (2005).
14. C. T. Dann and D. L. Garbers, "Production of knockdown rats by lentiviral transduction of embryos with short hairpin RNA transgenes," *Methods Mol. Biol.* **450**, 193–209 (2008).
15. T. Nakanishi, A. Kuroiwa, S. Yamada, A. Isotani, A. Yamashita, A. Tairaka, T. Hayashi, T. Takagi, M. Ikawa, Y. Matsuda, and M. Okabe, "FISH analysis of 142 EGFP transgene integration sites into the mouse genome," *Genomics* **80**(6), 564–574 (2002).
16. A. Onishi, M. Iwamoto, T. Akita, S. Mikawa, K. Takeda, T. Awata, H. Hanada, and A. C. F. Perry, "Pig cloning by microinjection of fetal fibroblast nuclei," *Science* **289**(5482), 1188–1190 (2000).
17. T. Wakai, S. Sugimura, K. Yamanaka, M. Kawahara, H. Sasada, H. Tanaka, A. Ando, E. Kobayashi, and E. Sato, "Production of viable cloned miniature pig embryos using oocytes derived from domestic pig ovaries," *Cloning Stem Cells* **10**(2), 249–262 (2008).
18. T. Kawarasaki, M. Otake, S. Tsuchiya, M. Shibata, K. Matsumoto, and N. Isobe, "Co-transfer of parthenogenotes and single porcine embryos leads to full-term development of the embryos," *Anim. Reprod. Sci.* **112**(1–2), 8–21 (2009).

19. H. Niwa, K. Yamamura, and J. Miyazaki, "Efficient selection for high-expression transfectants with a novel eukaryotic vector," *Gene* **108**(2), 193–199 (1991).
20. K. Yoshioka, C. Suzuki, A. Tanaka, I. M. Anas, and S. Iwamura, "Birth of piglets derived from porcine zygotes cultured in a chemically defined medium," *Biol. Reprod.* **66**(1), 112–119 (2002).
21. H. Inoue, T. Murakami, T. Ajiki, M. Hara, Y. Hoshino, and E. Kobayashi, "Bioimaging assessment and effect of skin wound healing using bone marrow-derived mesenchymal stromal cells with the artificial dermis in diabetic rats," *J. Biomed. Opt.* **13**(6), 064036 (2008).
22. M. Hara, T. Murakami, and E. Kobayashi, "In vivo bioimaging using photogenic rats: fate of injected bone marrow-derived mesenchymal stromal cells," *J. Autoimmun* **30**(3), 163–171 (2008).
23. S. J. Li, S. L. Yang, S. H. Zhao, B. Fan, M. Yu, H. S. Wang, M. H. Li, B. Liu, T. A. Xiong, and K. Li, "Genetic diversity analyses of 10 indigenous Chinese pig populations based on 20 microsatellites," *J. Anim. Sci. (Savoy, Ill.)* **82**(2), 368–374 (2004).
24. X. F. Zhao, N. Y. Xu, X. X. Hu, and N. Li, "Effects of microsatellite in the regulatory region of IGF 1 on growth traits in Jinhua swine," *Yi Chuan.* **29**(2), 206–210 (2007).
25. J. Zhao, G. J. Nie, J. Z. Zhang, X. L. Guo, and N. Y. Xu, "Influence of MyoG gene on reproductive trails in Jinhua pig," *Yi Chuan.* **27**(6), 893–8978 (2005).
26. M. Shibata, M. Otake, S. Tsuchiya, M. Chikyu, A. Horiuchi, and T. Kawarazaki, "Reproductive and growth performance in Jinhua pigs cloned from somatic cell nuclei and the meat quality of their offspring," *J. Reprod. Dev.* **52**(5), 583–590 (2006).
27. J. P. Bidanel, J. C. Caritez, and C. Legault, "Ten years experiments with Chinese pig in France.1. breed evaluation," *Pig News Info.* **11**, 345–348 (1990).
28. H. Yoshino, K. Hashizume, and E. Kobayashi, "Naked plasmid DNA transfer to the porcine liver using rapid injection with large volume," *Gene Ther.* **13**(24), 1696–1702 (2006).
29. Y. K. Kang, D. B. Koo, J. S. Park, Y. H. Choi, H. N. Kim, W. K. Chang, K. K. Lee, and Y. M. Han, "Typical demethylation events in cloned pig embryos. Clues on species-specific differences in epigenetic reprogramming of a cloned donor genome," *J. Biol. Chem.* **276**(43), 39980–39984 (2001).
30. K. Inoue, T. Kohda, J. Lee, N. Ogonuki, K. Mochida, Y. Noguchi, K. Tanemura, T. Kaneko-Ishino, F. Ishino, and A. Ogura, "Faithful expression of imprinted genes in cloned mice," *Science* **295**(5553), 297 (2002).
31. N. Ogonuki, K. Inoue, Y. Yamamoto, Y. Noguchi, K. Tanemura, O. Suzuki, H. Nakayama, K. Doi, Y. Ohtomo, M. Satoh, A. Nishida, and A. Ogura, "Early death of mice cloned from somatic cells," *Nat. Genet.* **30**(3), 253–254 (2002).
32. I. Wilmut, N. Beaujean, P. A. de Sousa, A. Dinnyes, T. J. King, L. A. Paterson, D. N. Wells, and Young Le, "Somatic cell nuclear transfer," *Nature (London)* **419**(6907), 583–586 (2002).
33. M. Kurome, H. Ueda, R. Tomii, K. Naruse, and H. Nagashima, "Production of transgenic-clone pigs by the combination of ICSI-mediated gene transfer with somatic cell nuclear transfer," *Transgenic Res.* **15**(2), 229–240 (2006).

Invited Paper

# Bio-luminescent imaging and characterization of organ-specific metastasis of human cancer in NOD/SCID mice

Nicole A.L. Chun [a] & Takashi Murakami*[a]
[a] Division of Bioimaging Sciences, Center for Molecular Medicine, Jichi Medical University, Tochigi, Japan 329-0498

## ABSTRACT

Many clinical evidences demonstrate that the sites of distant metastasis are not random and certain malignant tumors show a tendency to develop metastases in specific organs (e.g., brain, liver, and lungs). However, an appropriate animal model to characterize the metastatic nature of transplantable human cancer cell lines has not been reported well. Recent advances in bio-luminescent imaging (BLI) technologies have facilitated the quantitative analysis of various cellular processes in vivo. To visualize the fate of tumor progression in the living mice, we are constructing a luciferase-expressing human cancer cell library (including melanoma, colon, breast, and prostate cancer). Herein we demonstrate that the BLI technology in couple with a fine ultrasonic guidance realizes cancer cell-type dependent metastasis to the specific organs. For example, some melanoma cell lines showed frequent metastasis to brain, lungs, and lymph nodes in the mouse model. Notably, reflecting the clinical features of melanoma, breast, and prostate cancer, some of the cell lines showed preferential metastasis to the brain. Moreover, these cellular resources for BLI allow a high throughput screening for potential anti-cancer drugs. Thus, this BLI-mediated additional strategy with the luciferase-expressing cancer cell resources should promote many translational studies for human cancer therapy.

**Keywords:** Cancer metastasis, human cancer cell line, luciferase, ultrasound, luminescent imaging, cardiac injection

## 1. INTRODUCTION

The metastasis of tumor cells represents the primary source of clinical morbidity and mortality in the large majority of solid tumors. Appropriately, the word "metastasis" (from the Greek for "change in position") refers to cell movement: the migration of cancer cells to body parts distant from the primary tumor. Clinicians and pathologists have long known that this process is not random (1, 2). Metastasis occurs in certain organs more than to others depending on the origin of the primary tumor. For example, melanoma shows preferential metastasis to the brain, lung, liver, and skin, while prostate cancer cells tend to metastasize to bone, lung, liver, and brain. It is thought that organ selectivity of metastasis is determined by anatomic considerations of blood flow, by cell intrinsic properties (e.g., expression of specific receptors or altered cytoskeletal states that facilitate metastasis), and by organ intrinsic properties (e.g., local production of tumor enhancing growth factors). However, appropriate small animal models to characterize the metastatic nature of transplantable human cancer cell lines have not been reported well.

Small animals (mice, rats) provide the most common animal models used in studies of cancer metastasis (2, 3). In most studies involving small animals, cell injection has been conducted through the tail vein of small animals. Alternatively, a model of left thoracotomy with cardiac injection under direct visualization was employed (4). The former route is not an advantageous method for the true systemic delivery because most of the injected cells are trapped in the capillaries of the lung. The latter case is invasive and carries 10–15% mortality and the actual delivery site is not visualized (4). Thus, less invasive delivery methods to the whole body are needed and should likely play a significant role in optimization of future studies for cancer metastasis.

High-resolution ultrasonography (US) has been developed specifically for small animal imaging (5). This new US employs higher frequencies (25 to 40 MHz), which result in increased spatial resolution, allowing clear identification of areas of interest within the myocardial wall of small animals and permitting precise and site-directed cell injection.

*takmu@jichi.ac.jp; phone 81 285 58-7446; fax 81 285 44-5365

Reporters, Markers, Dyes, Nanoparticles, and Molecular Probes for Biomedical Applications II, edited by Samuel Achilefu, Ramesh Raghavachari, Proc. of SPIE Vol. 7576, 757606
 · doi: 10.1117/12.836807

Recent advances in imaging strategies that reveal cellular and molecular biological events in real-time facilitate our understanding of biological processes occurring in living animals. The development of molecular tags such as green fluorescent protein (GFP) from the jellyfish (*Aequorea victoria*) and luciferase from the firefly (*Photinus pyralis*) has precipitated a revolution over the past decade, allowing complex biochemical processes to be associated with the functioning of proteins in living cells (2, 6, 7). In particular, luminescence imaging offers important opportunities for the investigation of a variety of biological processes in living cells (7): bioluminescent reporters have significantly greater signal-to-noise ratios in mammalian tissues, and emitted light signals can be quantified in the context of intact animal using non-invasive assays.

Herein we will highlight that high-resolution US guidance can be used for accurate and reproducible cardiac cell injection and that metastatic fate of transplanted tumor cells can be followed non-invasively with optical bioluminescence imaging.

## 2. MATERIALS AND METHODS

### *2.1 Cells and animals*

Male and Female NOD C.B-17-Prkdc$^{scid}$/J (NOD/SCID) mice (8-12 wks old) were purchased from Charles River Japan. All experiments in this study were performed in accordance with the Jichi Medical University Guide for Laboratory Animals.

Cancer cell lines were obtained from the American Type Culture Collection (Rockville, MD) and the Health Science Research Resources Bank (Sennan, Osaka, Japan). Depending on the cell line, cells were maintained in either Dulbecco's modified Eagle's medium (DMEM, GIBCO, Gaithersburg, MD) with 10% heat-inactivated fetal calf serum (FCS) and supplements (8) or RPMI-1640 (GIBCO) with 10% FCS and supplements. The cultures were kept in a 5% $CO_2$ and 95% air humidified atmosphere at 37°C.

### *2.2 Establishment of luciferase-expressing cells*

Firefly (*Photinus pyralis*) luciferase cDNA from pGL3 basic (Promega, Madison, WI) was inserted into the pMSCVpuro retroviral vector (Clonetech), generating pMSCV-luciferase. GP2-293 packaging cells (Clontech) were cotransfected with pMSCV-luciferase and pVSV-G (Clontech), a plasmid encoding the viral envelope glycoprotein (VSV-G) of vesicular stomatitis virus, using Lipofectamine 2000 (Invitrogen). Supernatants from transfected GP2-293 were incubated with ~50% cells in the presence of Polybrene (8 mg/ml final concentration; Sigma-Aldrich). Transduced cells were propagated in medium containing puromycin (Sigma-Aldrich) at 15 mg/ml (Figure 1A). Established cells were listed on Figure 1B.

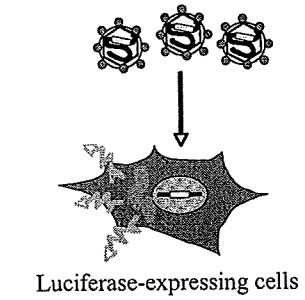


B

| Cell lines | Photon levels |
|---|---|
| *Gastric cancer* | |
| MKN-45 | good |
| MKN-1 | poor |
| KatoIII | poor |
| NUGC-3 | very good |
| *Breast cancer* | |
| MDA-MB-231 | very good |
| HS578T | very good |
| BT-549 | good |
| MCF7 | good |
| T-47D | very good |
| *Melanoma* | |
| SK-MEL-2 | very good |
| SK-MEL-28 | very good |
| COLO 679 | very good |
| Mewo | very good |
| MM-RU | very good |
| *Colon cancer* | |
| HT-29 | very good |
| KM12 | very good |
| SW620 | very good |
| HCT-116 | very good |
| COLO205 | poor |
| DLD-1 | good |
| LoVo | on going |
| *Prostate cancer* | |
| DU-145 | very good |
| PC-3 | very good |

*Figure 1. Construction of firefly luciferase-expressing human cancer cell lines.*

### *2.3 Xenogeneic cardiac tumor injection*

Luciferase (luc)-expressing cells in the exponential growth phase were harvested by trypsinization and washed twice in phosphate-buffered saline (PBS) before injection. Luc-expressing cells ($5 \times 10^5$ in 0.2 ml of PBS) were inoculated into the left cardiac ventricle of NOD/SCID mice under a fine ultrasonography (US) guidance. Briefly mice were anesthetized by inhalation of 1.5% isoflurane. The mice were then fixed in the supine position on a custom-built mold designed and their natural body shape was maintained (Figure 2A). The chest of the mice were shaved and further cleaned with a chemical hair remover to minimize ultrasound attenuation. Short-axis echocardiography was accomplished with a Vevo770 system (VisualSonics Inc., Toronto) in B mode with the use of a 700 series real-time micro-visualization (RMV) scan head probe (Model RMV 707B). Ultrasound gel was spread over the precordial region to visualize the left ventricle (Figure 2B). When the vertical-section with the largest left-ventricular chamber dimension was located, a cell suspension was loaded into a syringe fitted with a sterile disposable 30-gauge needle. The synringe was secured in a micromanipulator, and the needle and the RMV scanhead probe were aligned before the injection procedure (the needle angle was at ~ 45 degree to the table surface; see Figure 2A). Under the real-time image guidance, the needle was inserted into the left ventricle. The injection can be monitored on the ultrasound screen and documented as video clips on the Vevo770 computer.

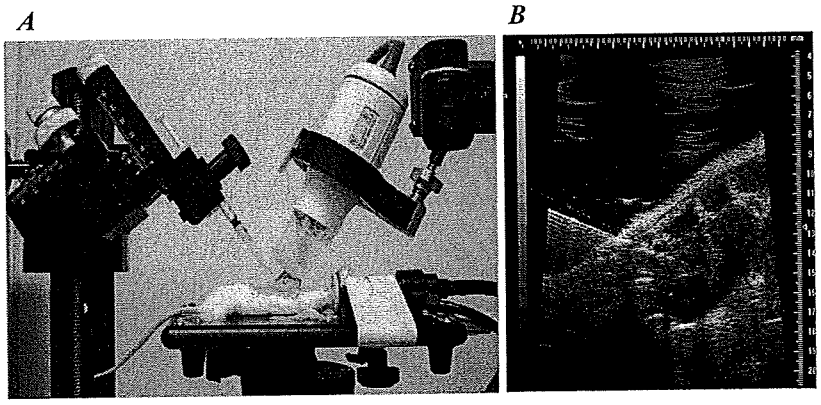


***Figure 2. The use of a high-resolution ultrasound (25-75 MHz) allows accurate cardiac cell injection.***

### *2.4 Histological examination*

Removed specimens were fixed with 10% paraformaldehyde and embedded in paraffin. Sections were then stained with hematoxylin-eosin.

### *2.5 In vivo luminescent imaging*

*In vivo* tumor progression was monitored using the non-invasive bioimaging system IVIS™ (Xenogen, Alameda, CA). Tumor-injected mice were anesthetized with Isoflurane (Abbott Laboratories, North Chicago, IL), and D-luciferin (potassium salt; Biosynth, Postfach, Switzerland) was injected into the peritoneal cavity (3 mg/body). Mice were immediately followed by the measurement of luciferase activity. The imaging system consisted of a cooled, back-thinned charge-coupled device (CCD) camera to capture both a visible light photograph of the animal taken with light-emitting diodes and the luminescent image. After acquiring photographic images of each mouse, luminescent images were acquired with a 1 min exposure time (9, 10). Images were obtained with a 25-cm field of view (FOV), a binning (resolution) factor of 8, 1/f stop, and an open filter. The resulting gray scale photographic and pseudo-color luminescent images were automatically superimposed using software to facilitate identification of any optical signal and location on the mouse. Optical images were displayed and analyzed using Igor (WaveMetrics, Lake Oswego, OR) and IVIS Living

Image (Xenogen) software packages. The signal from tumors was quantified as photons flux in units of photons/sec/cm$^2$/steradian.

### *2.6 Ex vivo luminescent imaging inspection*

For the inspection of metastasized organs, various organs of the mice were removed onto culture dishes and tumor-derived photons were examined for micro-metastases in the presence of D-luciferin (250 ug/mL). The following representative organs of mice were evaluated for the metastases: the lung, liver, brain, spine, paraaortic lymph nodes, gut and omentum, peritoneum, retroperitoneum, spleen and bladder.

## 3. RESULTS

### *3.1 Photon emission from luciferase-expressing cancer cells are correlated with viable cell number*

Recent advances in luminescent imaging technologies have facilitated the quantitative analysis of cellular processes *in vivo*. Human cancer cell lines were transduced with firefly luciferase in an effort to visualize the fate of tumor progression in the living animals. The advantages associated with the use of luciferase as a marker includes its sensitivity (as few as 100 luciferase-transduced cells can be detected over the background *in vitro*) and its linear dose-dependent output of light in the presence of D-luciferin (data not shown).

We have previously shown that depsipeptide induces apoptotic cell death in human melanoma cell lines (11, 12). We examined whether photon emission from luciferase-expressing tumor cells was correlated with viable cell number. A sublethal dose of depsipeptide on murine B16/F10 melanoma cells (Figure 3A) revealed that depsipeptide decreased tumor-derived photons in a dose-dependent manner. Furthermore, caspase-3/7 activity in unmanipulated B16/F10 cells also increased linearly after a 24 hr exposure to 1-10 nM depsipeptide (Figure 3B), with the median dose of depsipeptide ($ED_{50}$) being 5.34 nM. Thus, these data indicate that tumor-derived photons were correlated well with viable cell number.

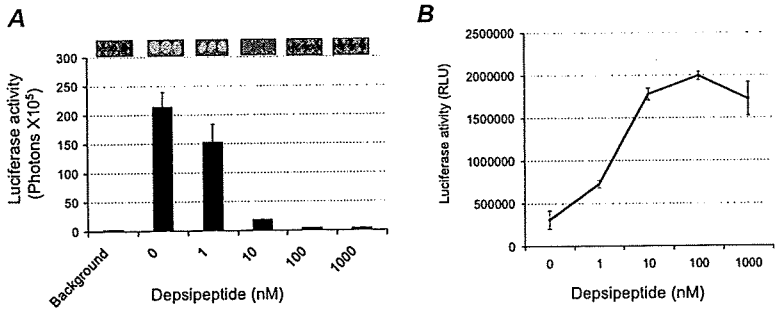


***Figure 3. Photon emission from luciferase-expressing cancer cells are correlated with viable cell number.*** (A) Luc-B16/F10 cells (1 x $10^5$) were plated onto 48-well plates at the indicated number and exposed to depsipeptide at the indicated concentration for 16 hr. Luciferase activity (photon counts) was then evaluated in the presence of D-luciferin. (B) Caspase-3/7 activity was quantified for 16 hr following treatment at the indicated concentration of depsipeptide in B16/F10 cells (2 x$10^4$). The Caspase-GloTM 3/7 Assay system (Promega, Madison, WI) was used according to the manufacturer's instructions. The background luminescence associated with the cell culture and assay reagent (blank reaction) was subtracted from experimental values.

### *3.2 Organ-specific metastasis of human cancer cells in NOD/SCID mice*

Luciferase-expressing cells were inoculated into the left cardiac ventricle of NOD/SCID mice under fine US guidance. BLI was conducted per cell line and representative organs (e.g. brain, liver, lungs, lymph nodes, bones and gastrointestinal tract) were followed by *ex vivo* inspection. In the case of human melanoma cell lines, their metastatic potential was dependent on the cell line (Figure 4A). For example, SK-MEL-2 cells showed a low metastatic phenotype, and SK-MEL-28 and Mewo cells had a moderate metastatic phenotype. Colo679 cells showed the most aggressive metastatic phenotype among the cell lines. SK-MEL-28, Mewo and Colo679 cells tend to metastasize to the brain, lungs, liver and lymph nodes of NOD/SCID mice (Figure 4B). These data indicate that metastatic potentials of melanoma to specific organs depend on the cell line.

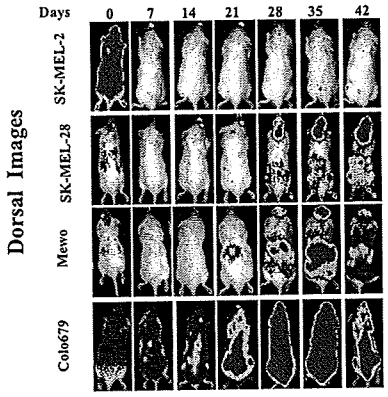


*Figure 4A. Melanoma cell lines - in vivo luciferase imaging*

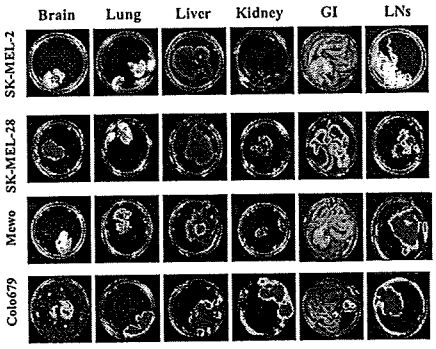


*Figure 4B. Ex vivoluminescent inspection*

We further investigated other cell lines. While human colon cancer HT-29 cells accumulated significantly in the liver of mice (Figure 5), breast cancer MDA-MB-231 cells showed bone metastasis in addition to metastasis to the brain, lungs and lymph nodes (Figure 6). These profiling data of hematogenous metastasis suggest that human cancer cell lines conserve their own favorite metastatic sites even in mice (beyond the species). Notably, reflecting the clinical features of melanoma and breast cancer, some of the cell lines showed preferential metastasis to the brain of NOD/SCID mice.

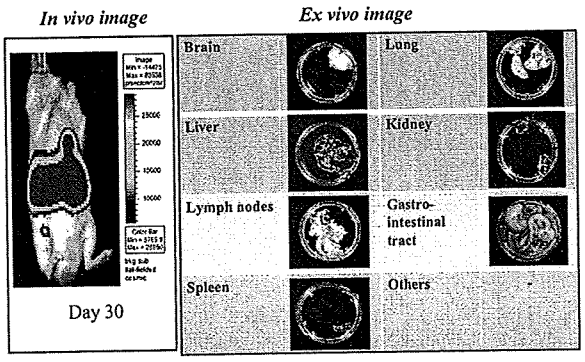


*Figure 5. Metastatic fate of luc-HT29 colon cancer cells*

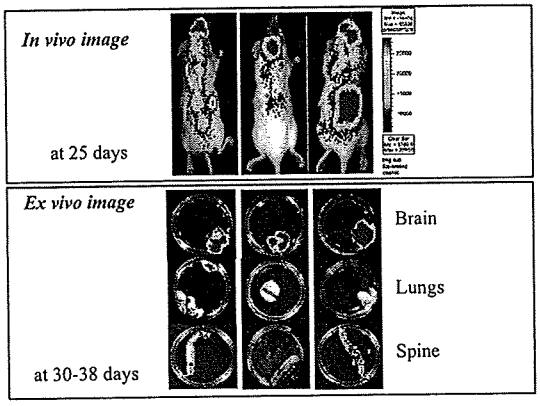


*Figure 6. Metastatic fate of luc-MDA-MB-231 breast cancer cells*

## 4. DISCUSSION

### *4.1 BLI for Cancer stem cells*

There appear to be characteristics common to both tumor cells and normal stem cells, referred to as *stemness*. The hallmark traits of stem cells—self-renewal and differentiation capacity—are reflected by the high proliferative capacity and phenotypic plasticity of tumor cells (13). Since the initial concept of cancer stem cells in solid tumor was established using NOD/SCID mice, we had to employ the animals to apply the luciferase-expressing cell resources to the theory of cancer stem cells. Our recent BLI-based experimentation suggested that a subpopulation of cancer stem cells is essential for organ-selective cancer metastasis (Figure 7).

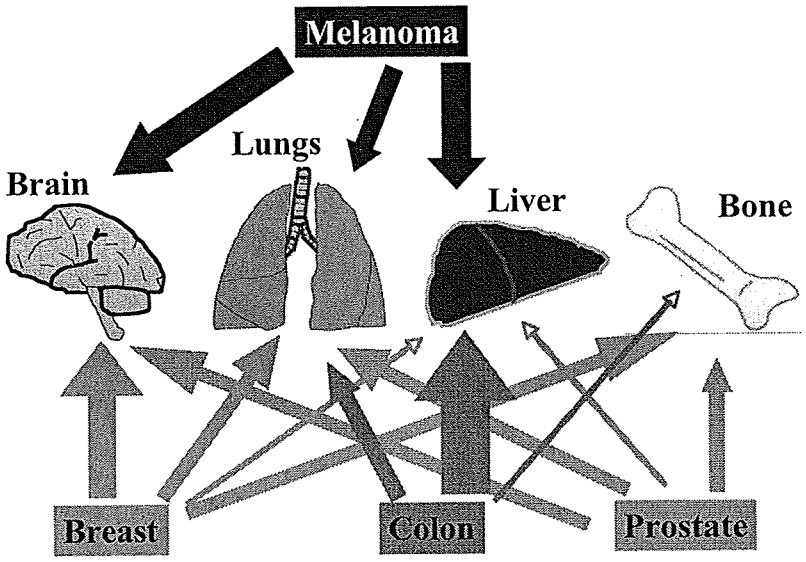


*Figure 7. Cancer cells appear to have their own favorite organs for metastasis*

### *4.2 Organ-specific cancer metastasis and chemokies*

Approximately 10–20% of all systemic malignancies will eventually metastasize to the brain (14). Despite the high frequency of metastatic brain tumors, there is no accepted paradigm for effective treatment. Accumulating clinical data suggest that the interaction between chemokines and their receptors is a critical component for regulation of tumor progression and metastasis in many cancer types (8, 15), and that the CXCR4/CXCL12 pathway is involved in the metastatic process (15). However, the pathophysiology in brain metastasis is not fully understood due to the difficulty of creating appropriate animal models. Therefore, BLI in conjunction with high-frequency US imaging should allow various preclinical studies at tumor-normal brain interfaces.

## 5. CONCLUSIONS

High-frequency ultrasound imaging can guide the injection of human cancer cells accurately into the left ventricle of mice, and applications of this technique for bio-luminescent imaging will elucidate the nature of hematogenous cancer metastasis. Combining cell resources with an appropriate animal model will promote a better and profound understanding of human cancer cell biology. However, progress always involves an innovative process. Therefore, advances in optical imaging should provide a new platform to accelerate development of therapeutic strategies for human cancer.

## ACKNOWLEDGMENTS

This study was supported by a grant to T.M. from the Health and Labour Science Research Grants from the Ministry of Health, Labor, and Welfare (Research on Biological Resources 08062877), and the Ministry of Education, Culture, Sports, Science and Technology (MEXT) of Japan, and by a grant from the "Strategic Research Platform" for Private Universities: matching fund subsidy from MEXT.

## REFERENCES

1. Nicolson, G. L., "Paracrine and autocrine growth mechanisms in tumor metastasis to specific sites with particular emphasis on brain and lung metastasis" Cancer Metastasis Rev 12, 325-343 (1993).
2. Sahai, E., "Illuminating the metastatic process," Nat Rev Cancer 7(10), 737-749 (2007).
3. Cranmer, L. D., Trevor, K. T., Bandlamuri, S., Hersh, E. M., "Rodent models of brain metastasis in melanoma," Melanoma Res 15(5), 325-356 (2005).
4. Wu, J.C., Chen, I. Y., Sundaresan, G., Min, J. J., De, A., Qiao, J. H., Fishbein, M. C., Gambhir, S. S., "Molecular imaging of cardiac cell transplantation in living animals using optical bioluminescence and positron emission tomography," Circulation 108(11), 1302-1305 (2003).
5. Foster, F. S., Pavlin, C. J., Harasiewicz, K. A., Christopher, D.A., Turnbull, D.H., "Advances in ultrasound biomicroscopy," Ultrasound Med Biol 26(1), 1-27 (2000).
6. Hoffman, R. M.,"The multiple uses of fluorescent proteins to visualize cancer in vivo," Nature Rev Cancer 5, 796-806 (2005).
7. Negrin, R.S., Contag, C.H., "In vivo imaging using bioluminescence: a tool for probing graft-versus-host disease," Nat Rev Immunol 6, 484-490 (2006).
8. Murakami, T., Maki, W., Cardones, A. R., Fang, H., Tun Kyi, A., Nestle, F. O., Hwang, S. T., "Expression of CXC chemokine receptor-4 enhances the pulmonary metastatic potential of murine B16 melanoma cells," Cancer Res 62, 7328-7334 (2002).
9. Sato, A., Ohtsuki, M., Hata, M., Kobayashi, E., Murakami, T., "Antitumor activity of IFN-lambda in murine tumor models," J Immunol 176, 7686-7694(2006).
10. Yanagisawa, S., Kadouchi, I., Yokomori, K., Hirose, M., Hakozaki, M., Hojo, H., Maeda, K., Kobayashi, E., Murakami, T., "Identification and metastatic potential of tumor-initiating cells in malignant rhabdoid tumor of the kidney," Clin Cancer Res 5, 3014-3022 (2009).
11. Kobayashi, Y., Ohtsuki, M., Murakami, T., Kobayashi, T., Sutheesophon, K., Kitayama, H., Kano, Y., Kusano, E., Nakagawa, H., Furukawa, Y., "Histone deacetylase inhibitor depsipeptide (FK228) suppresses the Ras-MAP kinase signaling pathway by up-regulation Rap1 and induces apoptosis in malignant melanoma," Oncogene 25, 512-524 (2006).
12. Murakami, T., Sato, A., Chun, N. A. L., Hara, M., Naito, Y., Kobayashi, Y., Kano, Y., Furukawa, Y., Kobayashi, E., "Transcriptional modulation using HDACi depsipeptide promotes immune cell-mediated tumor destruction of murine B16 melanoma," J Invest Dermatol 28(6), 1506-1516 (2008).
13. Reya, T., Morrison, S. J., Clarke, M. F., Weissman, I. L., "Stem cells, cancer, and cancer stem cells," Nature 414, 105-111 (2001).
14. Nussbaum, E. S., Djalilian, H. R., Cho, K. H., Hall, W. A., "Brain metastases. Histology, multiplicity, surgery, and survival," Cancer 78, 1781-1788 (1996).
15. Murakami, T., Cardones, A. R., Hwang, S.T., "Chemokine receptors and melanoma metastasis," J Dermatol Sci 36, 71-78 (2004).

# Functional molecular imaging of ILK-mediated Akt/PKB signaling cascades and the associated role of β-parvin

Mariko Kimura[1,2,*], Takashi Murakami[2,*], Shinae Kizaka-Kondoh[3], Masayuki Itoh[4], Keiji Yamamoto[1], Yukihiro Hojo[1], Makoto Takano[4], Kazuomi Kario[1], Kazuyuki Shimada[1] and Eiji Kobayashi[2]

[1]Division of Cardiovascular Medicine, Department of Medicine, [2]Division of Organ Replacement Research, Center for Molecular Medicine and [4]Division of Molecular Physiology and Biophysics, Department of Physiology, Jichi Medical University, Shimotsuke 329-0498, Tochigi, Japan
[3]Department of Molecular Oncology, Kyoto University Graduate School of Medicine, Kyoto 606-8507, Japan
*Authors for correspondence (mkimura@jichi.ac.jp; takmu@jichi.ac.jp)

*Accepted 2 December 2009*
*Journal of Cell Science 123, 747-755*

*doi:10.1242/jcs.052498*

## Summary

Visualization and quantification of the dynamics of protein-protein interactions in living cells can be used to explore the macromolecular events involved in signal transduction processes. In this study, functional molecular imaging using a luciferase-based complementation method demonstrated how the integrin-linked kinase (ILK)-mediated protein complex controls downstream signals. The luciferase complementation assay showed that Akt1 preferentially binds to β-parvin rather than to ILK within the complex. Moreover, photon flux from the interaction between β-parvin and Akt1 increased following serum stimulation, and the β-parvin–Akt1 interaction was dependent on phosphoinositide 3-kinase. Intriguingly, small interfering (si)RNA-mediated β-parvin knockdown increased photon flux from the interaction between ILK and Akt1, leading to stabilization of hypoxia-inducible factor-1α and increased expression of vascular endothelial growth factor-A. These data from functional molecular imaging demonstrated that β-parvin plays a regulatory role in the ILK-mediated Akt (also called protein kinase B) signaling cascades, suggesting that β-parvin might be a crucial modulator of cell survival.

**Key words:** β-parvin, Molecular imaging, Integrin-linked kinase, Hypoxia-inducible factor, Luciferase

## Introduction

Extracellular signaling is commonly mediated through mechanisms that rely on protein-protein interactions and protein phosphorylation. The dynamics of protein-protein interactions are often dependent on the activation of a particular signal transduction pathway. Even a single protein can affect various cellular functions by interacting with different partners in response to extracellular stimuli.

Recent advances in the development of molecular probes have enabled the visualization of many cellular processes and the detection of protein-protein interactions in living cells, advances typified by the fluorescence resonance energy transfer (FRET) system (Förster, 1959), in addition to complementary methods using fluorescence (Hu et al., 2002) or luminescence (Luker et al., 2004). These complementary methods designed to visualize protein-protein interactions have recently been employed in the screening of interaction partners and the potential semi-high-throughput analysis of small modulator molecules in protein complexes (Kerppola, 2006a; Kerppola, 2006b). In particular, luciferase-based complementation imaging enables sensitive real-time monitoring and quantitative analysis of protein interactions under various cellular conditions (Luker et al., 2004).

Integrins and their associated proteins mediate various intracellular signaling pathways involved in cytoskeletal remodeling and cellular processes such as cell proliferation, survival and differentiation. Integrin-linked kinase (ILK), PINCH and parvin(s) form heterotrimeric complexes that function as important regulators of integrin-mediated signaling. The complex comprising ILK, PINCH and parvins has been implicated in mediating intracellular signaling pathways through phosphorylation of the leading downstream molecule Akt (also known as protein kinase B; PKB) (Legate et al., 2006). ILK-dependent target phosphorylation is largely regulated by phosphoinositide 3-kinase (PI3K). Akt/PKB activation requires phosphorylation of Thr308 by PI3K-dependent kinase-1 (PDK1) (Alessi et al., 1997; Williams et al., 2000) and Ser473 by PDK2 [which is also known as hydrophobic motif kinase (HMK)] (Feng et al., 2004; Troussard et al., 2003). ILK is capable of controlling vascular endothelial growth factor (VEGF) transcription through Akt/PKB phosphorylation (Tan et al., 2004). ILK kinase activity is also stimulated by VEGF and other growth factors, as well as by cell adhesion to the extracellular matrix (Attwell et al., 2003).

Parvins are a family of proteins involved in linking integrins and their associated proteins with intracellular pathways that regulate actin cytoskeletal dynamics and cell survival. It includes actopaxin/CH-ILKBP/α-parvin (ParvA), affixin/β-parvin (ParvB) and γ-parvin (ParvG). ParvB localizes to focal adhesions and is involved in cell adhesion, spreading, motility and survival through interactions with its partners. ParvB accumulates and co-localizes with ILK in heart and skeletal muscle (Bendig et al., 2006; Yamaji et al., 2001). It can inhibit ILK activity and reverse some oncogenic effects in cancer cells (Mongroo et al., 2004). Furthermore, the physiological interaction of ILK with ParvB is thought to be essential in maintaining cardiac contractility (Bendig et al., 2006). Nonetheless, the precise role of ParvB and the mechanism controlling the association of ILK and ParvB remain to be delineated.

Journal of Cell Science

Herein, we demonstrate that luciferase complementation imaging provides a useful strategy for the instantaneous monitoring of protein-protein interactions under serum stimulation. Employment of this system enabled the detection of limited protein-protein interactions, showing that ParvB preferentially interacts with Akt1, and inhibits the interaction between ILK and Akt1 under normal cell culture conditions. ParvB knockdown using small interfering (si)RNA increased VEGF expression, with concomitant stabilized expression of hypoxia-inducible factor 1-α (HIF-1α). Based on these findings, we propose that ParvB functions as an upstream modulator of Akt/PKB through ILK, Akt/PKB and HIF-1α signaling.

## Results

### Fluorescence complementation assay for protein-protein interactions involving ILK and associated proteins

It has been demonstrated that ILK protein complexes play a crucial role in regulating gene transcription and cell-cell adhesion. Molecular complementation methods were employed in an effort to detect real-time protein-protein interactions of ILK protein complexes with ParvB, PINCH1 and Akt1 (Fig. 1A). A fluorescent (or luminescent) probe was split into N-terminal and C-terminal probe fragments, each of which was attached to the N terminus or C terminus of the target protein using a linker. The optimal combination for each target protein-protein interaction leads to integration of the N-terminal and C-terminal probe fragments and light is emitted (Fig. 1A, right panel). To determine the optimal pairs of plasmids, four expression plasmids were constructed for each target protein fused with fluorescent (monomeric Kusabira-Green: mKG) or luminescent (firefly luciferase: Luc) N-terminal or C-terminal probe fragments using a linker (Fig. 1B). Protein interactions were investigated for structural conformations comprising ILK and ParvB, ILK and PINCH1, ILK and Akt1, ParvB and Akt1, and PINCH1 and Akt1. As shown in Fig. 1C, eight combinations per pair were tested to determine the optimal conformation in the living cell. The appropriate pairs of constructed plasmids were then co-transfected into 293T cells, which were then inspected using a fluorescent microscope under excitation light. One optimal pair with respect to target protein interactions was selected from among the eight combinations based on signal intensity. The optimal pairs for an mKG probe were N-ILK-linker-mKGC and N-ParvB-linker-mKGN (Fig. 1B: construct type 2 for ILK and construct type 1 for ParvB), mKGC-linker-ILK-C and mKGN-linker-PINCH1-C (construct type 4 for ILK and construct type 3 for PINCH1), N-ILK-linker-mKGN and N-Akt1-linker-mKGC (construct type 1 for ILK and construct type 2 for Akt1), N-ParvB-linker-mKGC and mKGN-linker-Akt1-C (construct type 2 for ParvB and construct type 3 for Akt1). The numbers represent the same four types of plasmids as in Fig. 1B. The plasmids encoded an unrelated protein and single plasmids did not show substantial fluorescent signals (Fig. 1D, lower six panels). Whereas the combination of ILK with ParvB or PINCH1 gave steady fluorescent signals in the cytosol (Fig. 1D, upper left panels), the combination of ParvB with Akt1 yielded stronger fluorescent signals than those yielded by the combination of ILK with Akt1 (Fig. 1D, upper right panels). The combination of PINCH1 with Akt1 did not generate substantial fluorescent signals in this assay (data not shown). In an effort to confirm the interaction between ParvB and Akt1, we performed a GST pull-down assay. Although a direct interaction between ParvB and Akt had not been reported before this study, the GST pull-down assay demonstrated that ParvB interacts directly with Akt1 (Fig. 1E). These results suggest that ParvB preferentially interacts with Akt1 and that ParvB might serve as a connecting molecule for ILK-mediated Akt/PKB signal transduction.

### Luminescence complementation assay for protein-protein interactions involving ILK and associated proteins

Although a variety of methodologies have been developed for the investigation of protein interactions (Kerppola, 2006a; Kerppola, 2006b), the luciferase-based complementation assay system potentially enables straightforward and real-time quantitative analysis in living cells (Luker et al., 2004; Paulmurugan et al., 2002). As with the fluorescence complementation assay, polypeptide ends, which can adopt a broad range of intermolecular orientations, might be problematic in terms of luciferase complementation imaging (Kerppola, 2006a; Kerppola, 2006b). Optimal luciferase complementation was investigated based on results derived from fluorescence complementation assays (see Fig. 1). The optimal N- and C-terminal fragments of firefly luciferase cDNA (NLuc and CLuc, respectively) were isolated by PCR, in which NLuc and CLuc correspond to firefly luciferase amino acids 2-416 and 398-550, respectively (Luker et al., 2004). Four fusion constructs were generated for each target protein using the NLuc and CLuc cDNA fragments (see Fig. 1B). Luciferase activity was then investigated by examining target protein-protein interactions. Expression plasmid pairs were transiently transfected into 293T cells. For the control transfection, only NLuc or CLuc was employed. To determine which pair generated optimal luminescent signals, the relative luciferase activity for each target protein interaction was examined. As shown in Fig. 2A-D, the optimal pairs were as follows: NLuc-linker-ILK-C and CLuc-linker-ParvB-C (construct type 3 for ILK and construct type 4 for ParvB), CLuc-linker-ILK-C and NLuc-linker-PINCH1-C (construct type 4 for ILK and construct type 3 for PINCH1), NLuc-linker-ILK-C and N-Akt1-linker-CLuc (construct type 3 for ILK and construct type 2 for Akt1), and NLuc-linker-ParvB-C and CLuc-linker-Akt1-C (construct type 3 for ParvB and construct type 4 for Akt1). Numbers represent the same four types of plasmids as in Fig. 1B. Single plasmids fused with only NLuc or CLuc cDNA did not show substantial luminescent signals. In order to validate actual expression levels of ParvB and Akt1 protein, 2 μg of the constructed plasmid DNA was transfected into 293T cells seeded in 12-well plates. ParvB and Akt protein expression levels were analyzed by western blotting (supplementary material Fig. S1). N-terminally fused forms of Akt1 protein, NLuc-linker-Akt1-C and CLuc-linker-Akt1-C, were detected in two cleaved fragments. It has been demonstrated that Akt can be cleaved by recombinant caspase 3 at aspartic acid residues 108 and 119, resulting in the generation of a 44 kDa pleckstrin-homology (PH) domain deficient fragment (Bachelder et al., 2001; Rokudai et al., 2000). One fragment appeared to be the PH domain of Akt1 fused with a split-luciferase probe, which was detectable using anti-luciferase antibody, and the other seemed to be the kinase domain of Akt1. These data indicated that the appropriate plasmid pair exclusively provided optimal luminescent signals.

### Real-time quantitative analysis of protein-protein interactions using a luciferase-based luminescent complementation assay

In an effort to determine the kinetic pattern of the ILK-ParvB and ILK-PINCH1 interactions, each optimal pair of plasmids was transfected into 293T cells in a 24-well plate. Emitted photons were measured for 30 minutes at 30 second intervals in the presence of D-luciferin using a NightOwl charge-coupled device camera. Maximal luminescence emitted from each well was observed at five to ten minutes. The photon count derived from the association of ILK with ParvB displayed a larger increase than that derived from

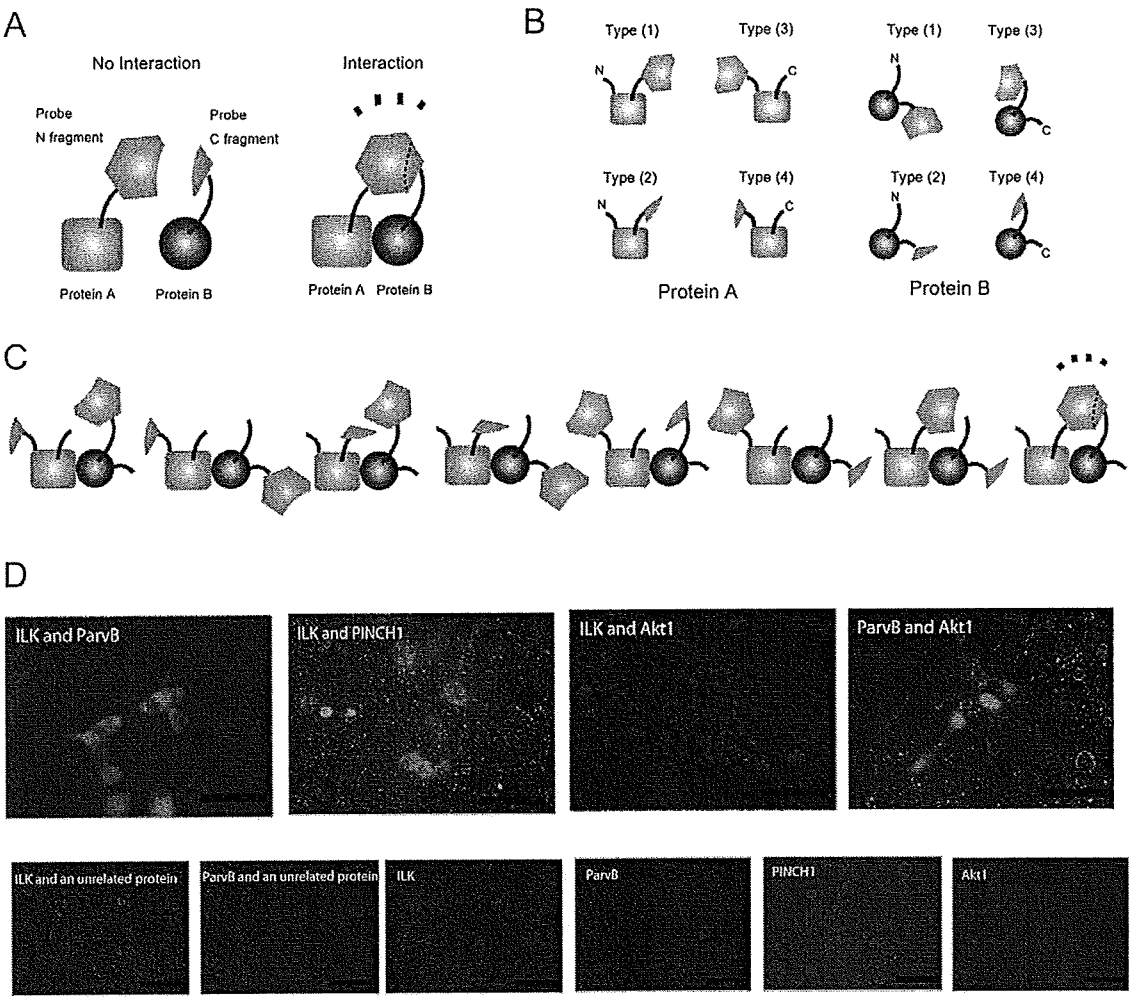


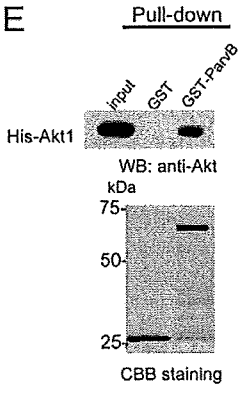


**Fig. 1. Complementation imaging strategy to investigate protein interactions of ILK, ParvB, PINCH1 and Akt1.** (A) Schematic representation of complementation methods used in this study. A fluorescent or luminescent probe was split into N- and C-terminal probe fragments that are fused with the N terminus or C terminus of either protein A or protein B (see Materials and Methods section). When protein A and protein B interact appropriately, the two probe fragments are reconstituted and light signal is emitted. (B) Constructed plasmids are theoretically classified into four types according to the linking position of the two probes. Four expression plasmids for each target protein (ILK, ParvB, PINCH1 and Akt1) have the same basic backbone that contains the N- or C-terminal fragments of the fluorescent or luminescent protein probe. (C) Schematic representation of the appropriate complementation pairs of plasmids. A potential eight combinations are employed to screen for optimum target protein-protein interactions. Based on four types of plasmid structures, the optimum combination needs to be determined as the indicated pair. (D) Optimized fluorescence signals were obtained for some complementation pairs of eight expression vectors pertaining to the target protein interactions. The optimized combination of ILK with ParvB, ILK with PINCH1, ILK with Akt1 and ParvB with Akt1 provided fluorescent signals in living 293T cells (upper panels). A related protein (NFκB1 p50 or RelA p65) with either ILK or ParvB, and the single plasmid alone (ILK, ParvB, PINCH1 and Akt1) did not give any fluorescent signals (lower panels). Scale bars: 100 μm. (E) GST pull-down assay. Glutathione-agarose beads coated with either GST or GST-ParvB were mixed with His-tagged Akt1, washed and detected by CBB staining and western blotting using anti-Akt antibody.

the association of ILK with PINCH1 at the maximum bioluminescent point (Fig. 3A,B).

Although ILK has been shown to bind to Akt (Persad et al., 2001), it had not been demonstrated that ParvB is associated with Akt1. The kinetics pertaining to the interaction of Akt1 with ILK or ParvB were therefore investigated. Optimal pairs of plasmids were transfected into 293T cells under the same conditions. As shown in Fig. 3C,D, the increase in photon flux derived from the association

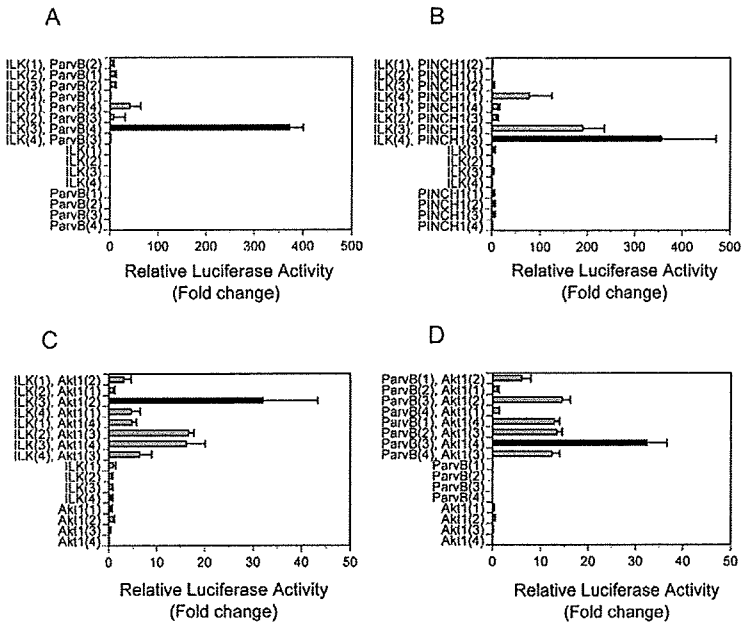


**Fig. 2. Relative luciferase activity in eight luciferase complementation pairs.** The optimized pair (black bar) found was for the following combinations: (**A**) ILK and ParvB, (**B**) ILK and PINCH1, (**C**) ILK and Akt1, (**D**) ParvB and Akt1. Numbers in parentheses represent the same four types of plasmids as in Fig. 1B.

of Akt1 with ParvB was much greater than that derived from the association of Akt1 with ILK, suggesting the preferential interaction of Akt1 with ParvB rather than ILK under living cell conditions. Maximum luminescent levels derived from the association of Akt1 with ParvB were in the range 800-1600 counts/pixels (50- to 100-fold higher than that observed for Akt1 and ILK). Kinetic analysis of Akt1-ILK complex formation showed an upward-bulging curve, with maximum luminescence levels being observed for 40-50 minutes following the addition of D-luciferin. Control expression using intact luciferase reached a peak immediately following the addition of D-luciferin (supplementary material Fig. S2). These results indicate that real-time complementary imaging can reveal

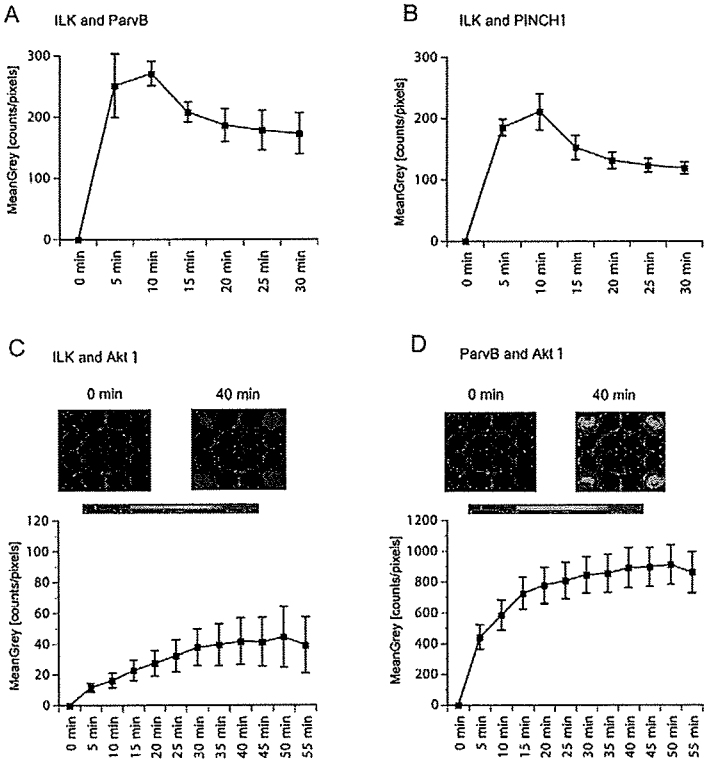


**Fig. 3. Kinetic luminescence signals of the optimal luciferase complementation pair in 293T cells.** (**A**) ILK and ParvB, (**B**) ILK and PINCH1, (**C**) ILK and Akt1, (**D**) ParvB and Akt1. The complementation imaging assay was performed under the same conditions pertaining to panels A and B, or C and D. With respect to Akt1-ILK and Akt1-ParvB complex formation, representative pseudo-color images (four-part) of a 24-well plate showed maximal luminescence signals 40 minutes following the addition of D-luciferin (upper panels). Notably, the combination of ParvB with Akt1 provided stronger signals than the combination of ILK with Akt1.

characteristics unique to each target protein-protein interaction, in this case suggesting that ParvB might be an important connecting molecule in the ILK-Akt/PKB signaling pathway.

### Functional complementation imaging demonstrated ParvB-Akt1 interaction following serum stimulation

In an effort to glean insight into the role of ParvB, we set out to determine whether the ParvB-Akt1 interaction was modified following serum-triggered induction. As depicted in Fig. 4A, representative pseudo-color images based on the split luciferase system revealed that photon flux derived from the interaction of ParvB with Akt1 increased under serum-rich conditions and diminished under serum-starved conditions or in the presence of a PI3K inhibitor. Consistent with these findings were the results obtained when investigating the kinetics of the ParvB-Akt1 interaction under serum-starved conditions or in the presence of a PI3K inhibitor with serum at 1-minute intervals following the addition of D-luciferin (Fig. 4B-D). The kinetic curves were logarithmic in shape. Maximum photon flux for the ParvB-Akt1 interaction for each condition was observed 20-40 minutes following serum stimulation. Serum-rich treatment increased photon flux derived from the interaction of ParvB with Akt1 (Fig. 4B). PI3K inhibitors such as LY294002 and wortmannin suppressed serum-triggered induction (Fig. 4C,D). Employment of a dual-luciferase assay also demonstrated that luciferase activity arising from the ParvB-Akt1 interaction in lysate cells was similar to photon flux in live cells (Fig. 4E). However, with respect to the ILK-Akt1 interaction and a control plasmid encoding full-length firefly luciferase, there was no significant change in luciferase activity under serum-starved or PI3K inhibitor conditions with serum (supplementary material Fig. S3A,B). These results demonstrate that serum stimulation increases photon flux derived from the interaction of ParvB with Akt1, suggesting that PI3K inhibitors attenuate the serum-stimulated interaction between ParvB and Akt1.

### Interaction between ILK and Akt1 is affected by ParvB mRNA levels

Because ILK-dependent phosphorylation is regulated by PI3K, it is possible that the inhibition of PI3K activity decreases ILK activity, which subsequently impairs the phosphorylation of putative ILK substrates (Delcommenne et al., 1998). One reliable marker that relates to ILK activity concerns the phosphorylation levels of Akt/PKB (Legate et al., 2006). Given the preferential association of ParvB with Akt1, we set out to determine whether ParvB levels regulate the interaction between ILK and Akt1. NIH3T3 cells were transfected with a reporter plasmid encoding the optimal split-luciferase complementation pair ILK-ParvB (Fig. 5A) and then subjected to siRNA-mediated ParvB knockdown. The knockdown efficiency of two types of mouse ParvB siRNAs (ParvB1 and ParvB2) is shown in Fig. 5B. These siRNAs were transfected into NIH3T3 cells stably overexpressing the complementation plasmid pair ILK-ParvB (see Fig. 5A) and the luminescence photon kinetics were evaluated (Fig. 5B). ParvB knockdown using siRNA decreased photon emission associated with ILK-ParvB association (siRNA ParvB2 was able to reduce approximately 50% of the photons derived from the interaction of ParvB with ILK). We then evaluated the extent of ILK-Akt1 complex formation with loss of ParvB using both luciferase complementation imaging and a co-immunoprecipitation assay. 293T cells were transfected with the optimal complementation plasmid pair ILK-Akt1 and then subjected to ParvB knockdown using siRNA ParvB2. As depicted in Fig. 5C,

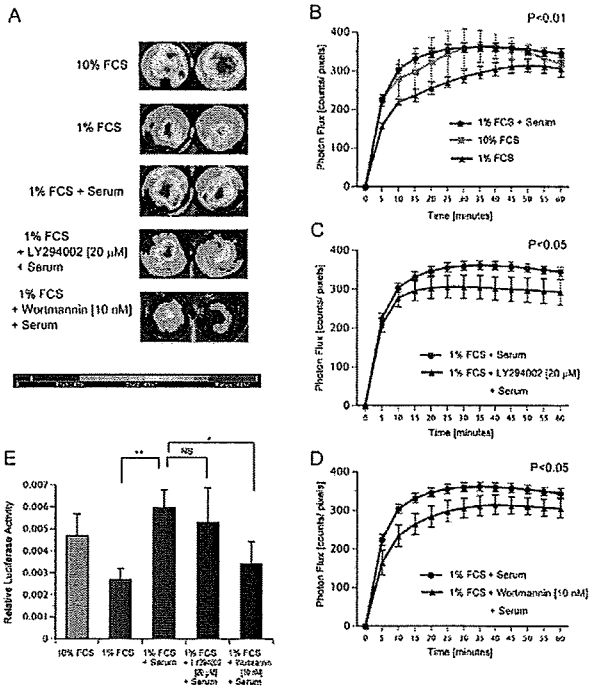


**Fig. 4. Kinetics of luciferase complementation imaging for ParvB-Akt1 complex formation under different conditions.** (**A**) Representative pseudo-color luminescence images emitted by the interaction between ParvB and Akt1 under either serum-starved conditions or in the presence of PI3K inhibitor (LY294002 or wortmannin) 20 minutes following serum stimulation. (**B**) Kinetic interaction between ParvB and Akt1 under serum-starved conditions following serum stimulation. 1% FCS versus 1% FCS plus serum. (**C,D**) Kinetic interaction between ParvB and Akt1 in the presence of PI3K inhibitors following serum stimulation: (C) 20 μM LY294002; (D) 10 nM wortmannin. 1% FCS plus serum versus 1% FCS plus serum plus PI3K inhibitor. (**E**) Relative luciferase activity for the interaction between ParvB and Akt1 20 minutes post-serum stimulation with or without PI3K inhibitors (LY294002 or wortmannin) All data are presented as a mean ± s.d. determined from the analysis of more than three independent experiments. NS, not statistically significant, $^{**}P<0.01$, $^{*}P<0.05$, ANOVA followed by post hoc tests or Student's *t*-test.

we investigated the kinetics of photons derived from the interaction of ParvB with Akt1 under ParvB knockdown conditions at 1-minute intervals following serum stimulation. Interestingly, siRNA ParvB led to an increase in photon flux associated with the ILK-Akt1 interaction. To provide further evidence showing that ParvB might regulate the ILK-Akt interaction, we performed a co-immunoprecipitation assay. 293T cells were transfected with the luciferase complementation plasmid pair ILK-ParvB (Fig. 5A) and then subjected to ParvB knockdown using siRNA ParvB2 (Fig. 5B). Overexpressed ILK and ParvB were precipitated with anti-phospho-Akt (Ser473) antibodies and precipitates were analyzed by western blotting using antibodies against ILK, ParvB, total-Akt and phospho-Akt (Ser473). As shown in Fig. 5D, decreased ParvB protein levels resulted in increased interaction between ILK and phospho-Akt (Ser473). These results suggest that ParvB might act as a potential modulator of the signal transduction associated with the ILK-Akt/PKB complex.

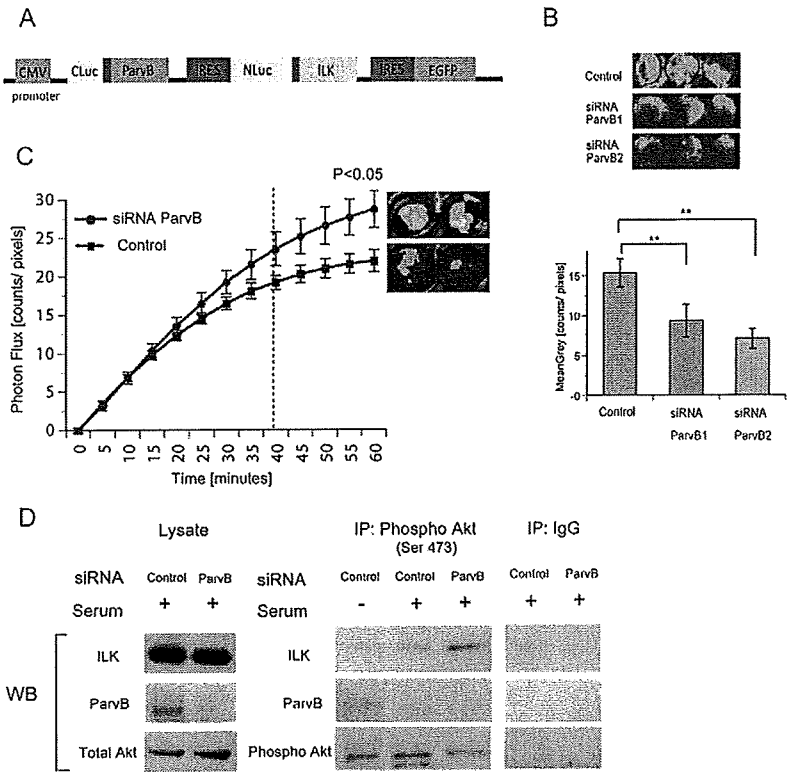


**Fig. 5. Interaction between ILK and Akt1 under ParvB knockdown conditions.** (**A**) Schematic representation of one expression vector encoding the optimal luciferase complementation pair ILK and ParvB. (**B**) ParvB knockdown by siRNA-inhibited luminescence signals in NIH3T3 cells overexpressing the optimal luciferase complementation pair ILK and ParvB. Representative pseudo-color images (triplicate) of a 24-well plate (the upper panel) and its quantification (the lower panel). (**C**) 293T cells were transfected with the optimal luciferase complementation plasmid pair ILK and Akt1, and then treated with ParvB siRNA. The graph represents photon-derived kinetics of the interaction between ILK and Akt1 following serum stimulation (left panel). Representative pseudo-color luminescence images (right panel) of a 12-well plate 40 minutes post-stimulation (broken line). (**D**) The plasmid encoding the optimal luciferase complementation pair ILK and ParvB (A) was transfected into 293T cells, and cells were then treated with ParvB siRNA. Cell lysates were precipitated (IP) using anti-phospho-Akt (Ser473) antibodies and control IgG antibody, and then subjected to western blotting (WB) using anti-ILK, anti-ParvB, anti-Akt and anti-phospho-Akt (Ser473) antibodies. All data are presented as a mean ± s.d. (***P*<0.01, ANOVA followed by post hoc tests or Student's *t*-test).

### ParvB knockdown increased HIF-1 and VEGF-A expression levels

We showed above that ParvB protein levels regulate the ILK-Akt1 interaction following serum stimulation. It has been demonstrated that HIF-1α is an important downstream effector that acts through the PI3K-Akt/PKB signaling pathway (Jiang et al., 2001). Furthermore, HIF-1α can regulate the expression of VEGF (Forsythe et al., 1996; Liu et al., 1995). In an effort to examine the effect of ParvB downregulation on downstream targets of the ILK-Akt signaling pathway, HIF-1α and VEGF protein expression levels were investigated following siRNA-mediated ParvB knockdown. ParvB is ubiquitously expressed, but enriched in heart and skeletal muscle (Bendig et al., 2006; Sepulveda and Wu, 2006). We transfected rat ParvB-specific siRNA into rat cardiomyocytes and confirmed the knockdown effect of ParvB (Fig. 6A). Western blot analysis demonstrated increased expression levels of endogenous HIF-1α and VEGF-A with ParvB knockdown in rat cardiomyocytes. HIF-1α and VEGF-A expression levels were quantified and statistically analyzed (Fig. 6B,C).

In an effort to further investigate the increase in HIF-1α expression induced by siRNA ParvB, another reporter plasmid was employed containing oxygen-dependent degradation (ODD)-luciferase, which comprises the ODD domain of HIF-1α fused to luciferase. Because the stability of HIF-1α is tightly regulated through the ODD domain (Harada et al., 2002), luciferase activity associated with the fusion protein reflects stabilized HIF-1α levels. ODD-luciferase cDNA was subcloned into the pcDNA3.1 expression plasmid (Fig. 6D) and transfected into NIH3T3 cells. ODD-luciferase-expressing stable transformants were obtained following G418 selection. We then introduced siRNA ParvB1 or ParvB2 into the ODD-luciferase-expressing NIH3T3 transformants. As shown in Fig. 6E, ParvB knockdown resulted in a marked increase in the expression of ODD-luciferase. Moreover, the hypoxia mimetics $CoCl_2$ and desferrioxamine (DFO) also increased ODD-luciferase-derived photon flux in the NIH3T3 transformants (Fig. 6F). To further confirm the requirement for ILK in the induction of HIF-1α stability under loss of ParvB, both siRNA ParvB1 and siRNA ILK were introduced into ODD-luciferase-expressing NIH3T3 transformants. As shown in Fig. 6G, knockdown using both ParvB and ILK did not increase ODD-luciferase-derived photon flux in the NIH3T3 transformants (Fig. 6G).

Taken together, these results indicate that decreased levels of ParvB stabilize HIF-1α in the presence of ILK, suggesting that ParvB downregulation might mimic hypoxic conditions through the ILK-Akt/PKB signaling pathway.

## Discussion

Complementation strategies using an imaging probe with appropriate protein reconstitution enable visualization of steady-state complexes formed between protein pairs. One of the benefits associated with the use of these techniques is the exclusion of certain secondary effects or potential artifacts caused by cell lysis (Kerppola, 2006a; Kerppola, 2006b). Of the available complementation strategies, luciferase-based luminescence complementation imaging can be employed as a facile and broadly applicable approach (Luker et al., 2004). In this study, we demonstrated two complementary methods employing fluorescent or luminescent protein probes. Both imaging methods required that eight combinations of reporter plasmids be examined to determine optimal signal gain from the target protein-protein interaction.

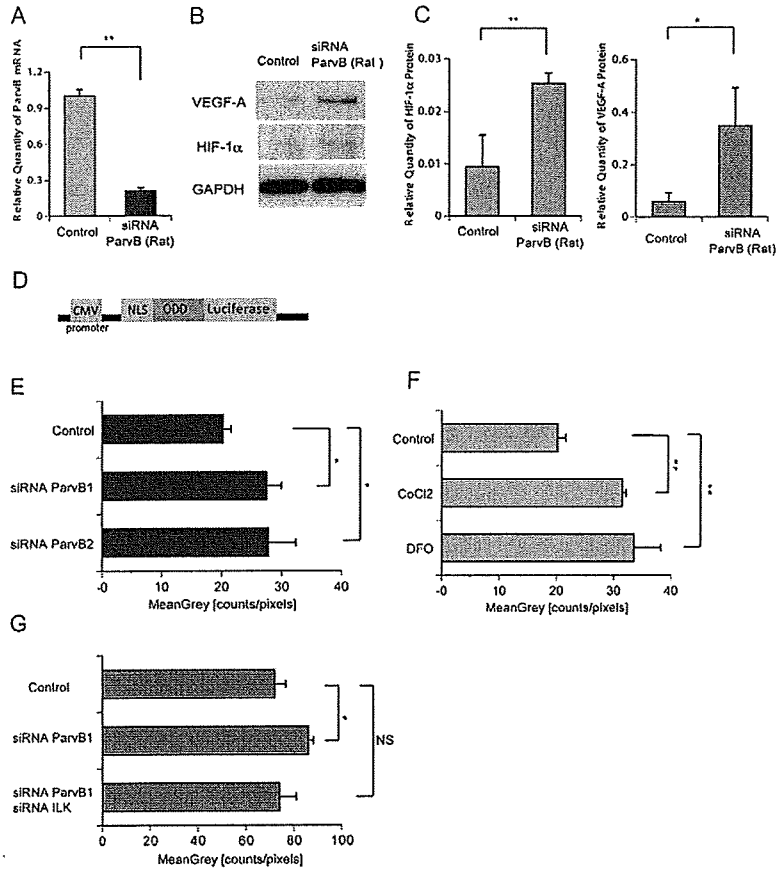


**Fig. 6. Stabilization of HIF-1 and increased expression of VEGF-A under loss of ParvB.** (**A**) Quantitative real-time RT-PCR for ParvB in rat cardiomyocytes following treatment with rat ParvB-specific siRNA. (**B**) siRNA-mediated ParvB knockdown increased protein expression levels of HIF-1α and VEGF-A in cardiomyocytes following serum stimulation. (**C**) Quantitative analysis (using ImageJ software) of endogenous HIF-1α (left panel) and VEGF-A (right panel) expression levels from the siRNA-mediated ParvB knockdown experiments shown in B. (**D**) Schematic representation of the reporter plasmid construct encoding a fusion protein, ODD-luciferase, which comprises part of the ODD domain of HIF-1α fused to luciferase (Harada et al., 2002). (**E**) siRNA-mediated ParvB knockdown increased photon count in NIH3T3 cells overexpressing ODD-luciferase. (**F**) Hypoxia mimetics $CoCl_2$ (100 μM) and DFO (20 μM) increased luminescent signals in NIH3T3 cells overexpressing ODD-luciferase. (**G**) Double-knockdown using ParvB- and ILK-specific siRNAs did not increase ODD-luciferase-derived photons in the NIH3T3 transformants. All data are presented as a mean ± s.d. determined from the analysis of more than three independent experiments (**$P$<0.01, *$P$<0.05, ANOVA followed by post hoc tests or Student's $t$-test).

Although fluorescence complementation enabled visual observation of the actual protein interactions, it might not necessarily allow comparison of protein-protein interactions in living cells under the microscope. By contrast, luminescence complementation enables comparison of even weak protein interactions under almost real-time conditions by quantifying luminescent signals with a high signal-to-noise ratio. Furthermore, employment of the luciferase complementation strategy allows the observation of rapid changes in target protein interactions in subcellular compartments under various conditions. In fact, our extensive complementary studies demonstrated that ParvB preferentially binds to Akt1 rather than ILK under living cell conditions. Moreover, luciferase complementation imaging revealed that real-time changes in photon-based kinetics associated with the ParvB-Akt1 interaction were consistent with results obtained following the use of extracellular stimuli, such as growth factors and associated signal inhibitors. Thus, employing the complementation strategy with appropriate probes could provide unique findings that reflect real-time cellular responses to external stimuli. Based on the current studies, employment of functional molecular imaging using complementary methods promises to be a beneficial strategy for the exploration of molecular mechanisms pertaining to signal transduction.

The ILK-associated protein complex is profoundly involved in altering the flux of the PI3K-Akt/PKB signaling pathway (see Fig. 7). ILK-dependent phosphorylation is regulated in a PI3K-dependent manner. PI3K inhibitors reduce ILK activity and impair the phosphorylation of putative ILK substrates in cell culture (Delcommenne et al., 1998). ParvB is a binding partner of ILK and the CH2 domain of ParvB is phosphorylated by ILK. These findings suggest that ParvB probably plays a role in actin cytoskeleton remodeling and cell spreading with its binding partners, α-actinin and αPIX (Mongroo et al., 2004; Yamaji et al., 2004; Yamaji et al., 2001). One new finding in our study showed that the real-time photon-based kinetics of the ParvB-Akt interaction correlated with results obtained following the use of extracellular stimuli, such as the presence of serum with or without PI3K inhibitors (Fig. 4). Moreover, decreased levels of ParvB protein were associated with a marked increase in photons derived from the ILK-Akt interaction (Fig. 5C,D). Although the interaction between ParvB and Akt had not been reported before this study, ParvB might cooperate with Akt and play a regulatory role in ILK-Akt complex formation (Fig. 7).

The role of ParvB in relation to Akt/PKB downstream effectors had not previously been sufficiently addressed. In this study, we demonstrated that siRNA-mediated ParvB knockdown increased HIF-1α and VEGF expression in rat cardiomyocytes (Fig. 6B,C). In particular, we showed that the phenomenon was correlated with HIF-1α stabilization. In our luciferase-based real-time imaging, ODD-luciferase expression levels increased with siRNA-mediated ParvB knockdown, firmly supporting the notion of HIF-1α stabilization (Fig. 6E). Furthermore, the hypoxia mimetics $CoCl_2$ (100 μM) and DFO (20 μM) increased luminescent signals in ODD-luciferase-overexpressing NIH3T3 cells. The effect of ParvB knockdown was the same as that of hypoxia mimetic agents. However, knockdown using both ParvB and ILK siRNAs did not increase luminescent